

The Relationship Between Visual Sensitivity and Eccentricity, Cone Density and Outer Segment Length in the Human Foveola

Niklas Domdei, Jenny L. Reiniger, Frank G. Holz, and Wolf M. Harmening

Department of Ophthalmology, Rheinische Friedrich-Wilhelms-Universität Bonn, Bonn, Germany

Correspondence: Wolf M. Harmening, Department of Ophthalmology, Rheinische Friedrich-Wilhelms-Universität Bonn, Sigmund-Freud-Strasse 25, 53127 Bonn, Germany; wolf.harmening@ukbonn.de.

Received: April 12, 2021

Accepted: June 17, 2021

Published: July 21, 2021

Citation: Domdei N, Reiniger JL, Holz FG, Harmening WM. The relationship between visual sensitivity and eccentricity, cone density and outer segment length in the human foveola. *Invest Ophthalmol Vis Sci.* 2021;62(9):31. <https://doi.org/10.1167/iovs.62.9.31>

PURPOSE. The cellular topography of the human foveola, the central 1° diameter of the fovea, is strikingly non-uniform, with a steep increase of cone photoreceptor density and outer segment (OS) length toward its center. Here, we assessed to what extent the specific cellular organization of the foveola of an individual is reflected in visual sensitivity and if sensitivity peaks at the preferred retinal locus of fixation (PRL).

METHODS. Increment sensitivity to small-spot, cone-targeted visual stimuli (1 × 1 arcmin, 543-nm light) was recorded psychophysically in four human participants at 17 locations concentric within a 0.2° diameter on and around the PRL with adaptive optics scanning laser ophthalmoscopy-based microstimulation. Sensitivity test spots were aligned with cell-resolved maps of cone density and cone OS length.

RESULTS. Peak sensitivity was at neither the PRL nor the topographical center of the cone mosaic. Within the central 0.1° diameter, a plateau-like sensitivity profile was observed. Cone density and maximal OS length differed significantly across participants, correlating with their peak sensitivity. Based on these results, biophysical simulation allowed to develop a model of visual sensitivity in the foveola, with distance from the PRL (eccentricity), cone density, and OS length as parameters.

CONCLUSIONS. Small-spot sensitivity thresholds in healthy retinas will help to establish the range of normal foveolar function in cell-targeted vision testing. Because of the high reproducibility in replicate testing, threshold variability not explained by our model is assumed to be caused by individual cone and bipolar cell weighting at the specific target locations.

Keywords: psychophysics, microstimulation, adaptive optics, sensitivity, morphology

The central part of the human retina, the fovea, features several morphologic specializations as a result of a complex series of events that are initiated during gestation and completed in childhood.^{1,2} The network of retinal blood vessels organizes itself around an avascular zone concentric within the fovea,³ and the foveal pit emerges as post-receptoral neurons migrate laterally. As a consequence, the foveola, the central 0.6° diameter of the fovea,⁴ is completely free of overlying neural tissue, favoring undisturbed light catch. Cone photoreceptors migrate inward to form a lattice of tightly packed receptors at their smallest diameter found anywhere in the retina,⁵ and simultaneously the pigment-laden cone outer segments (OSs) elongate,¹ leading to a peak in optical density at the foveola.^{6,7} At close inspection, the topography and density of cone photoreceptors within the foveola are highly variable among individuals^{8,9} and it is not clear to what extent the individual cellular mosaic and the exact foveal topography is related to visual sensitivity.

On a broader scale, photopic light sensitivity is best at the fovea¹⁰ and drops rapidly with increasing eccentricity.¹¹ Several clinical studies using fundus-guided perimetry, so-called microperimetry, have investigated the structure-function relationship in the fovea of diseased eyes and

observed a correlation between retinal thickness and sensitivity.^{12–14} The application of adaptive optics to determine foveal cone spacing of patients with retinal degeneration revealed a correlation between foveal sensitivity and cone spacing.^{15–18} These studies faced two key limitations. First, foveal sensitivity was tested at a single location and compared across patients, not across retinal space within an individual. Second, stimulus size (Goldmann III, ~26 arcmin diameter) was large compared with a minimal cone spacing of about 0.5 arcmin.⁵ Sensitivity to luminance stimuli is assumed to be conveyed primarily by parasol ganglion cells.¹⁹ This view is supported by the observation that spatial summation is correlated with the dendritic field size of parasol ganglion cells.²⁰ In the foveola, however, the diameter of the spatial summation area was found to be about 2.5 arcmin and therefore between the dendritic field size of parasol and midget ganglion cells.²¹ Thus, a visual stimulus at the same size or even smaller than this spatial summation area is crucial to reveal an otherwise conflated relationship between the peaking topography of the detector array in the foveola and its visual sensitivity.

Concomitant to the peaking spatial sampling capacity at the fovea, motor circuits of the brain stem generate eye



and head movements to bring the retinal images of objects of interest detected in the periphery into the foveola,^{22,23} where they fall on a distinct bouquet of only a handful of cones, the preferred retinal locus of fixation (PRL), or “optimal locus”, of fixation.^{24–26} In clinical research, the term PRL refers to a newly formed stable location on the retina used for fixation,²⁷ due to a central scotoma^{28–31} caused by macular diseases,³² such as age-related macular degeneration.³³ Classical work assumed that, in healthy participants, this location might colocalize with the location of peak cone density.^{25,34,35} With high-resolution *in vivo* imaging, it has now been shown, also in healthy participants, that the PRL is offset from the location of peak cone density,²⁶ the center of the bottom of the foveal pit³⁶ or the center of the foveal avascular zone.^{37–39} The underlying processes of PRL formation are yet unknown, and the newly formed PRL in patients is usually a suboptimal retinal location, given the fact that other intact locations of the retina would have provided better acuity⁴⁰ or higher contrast sensitivity.³³ Here, we hypothesized that the subset of cones at the PRL may have functional preeminence in terms of visual sensitivity, as fixational eye movements re-center the object of interest onto this location with extreme precision.^{9,41}

With recent optical tools, the mosaic of even the smallest cone photoreceptors in the foveola can now be resolved in the living human eye, and visual function such as visual sensitivity can be simultaneously probed psychophysically with cellular precision.⁴² In a first attempt to better understand how the morphological factors such as distance from the PRL, cone density, and OS length have functional consequences on vision, we used this experimental access to study the direct relationship between the cellular makeup of the foveal center and sensitivity to light in four healthy human participants.

METHODS

In four human participants (one female; ages 29, 32, 42, and 42 years), the cellular topography of the fovea, light sensitivity to cone-sized stimuli, and PRL were mapped with cellular precision using an adaptive optics scanning laser ophthalmoscope (AOSLO) microstimulator. The participants were three of the authors (P1 = N.D., P2 = J.L.R., P3 = W.M.H.) and one lab member (P4). Pupil dilation and cycloplegia were induced by instilling 1 drop of 1% tropicamide 15 minutes before the beginning of an experimental session. For each participant, a custom dental impression (bite bar) was used to immobilize and control the position of the head during imaging and stimulation. Written informed consent was obtained from each participant, and all experimental procedures adhered to the tenets of the Declaration of Helsinki, in accordance with the guidelines of the independent ethics committee of the medical faculty at the Rheinische Friedrich-Wilhelms-Universität of Bonn, Germany.

AOSLO Microstimulator

The central $\sim 1^\circ$ of the right eye of each participant was imaged, and targeted test sites were simultaneously stimulated with a custom multiwavelength AOSLO.^{43–46} In brief, one near-infrared (IR) light channel was used for imaging and wavefront sensing (840 ± 12 nm; FF01-840/12-25, Semrock, Rochester, NY, USA), and a visible green light channel was used for stimulation (FF01-543/22-25, 543 \pm 22 nm;

Semrock), which is thought to stimulate the L- and M-cone photopigments equally, based on their absorbance.⁴⁷ Adaptive optics correction, run in a closed loop at about 25 Hz, consisted of a Shack-Hartmann wavefront sensor (SHSCam AR-S-150-GE; Optcraft GmbH, Erlangen, Germany) and a magnetic 97-actuator deformable mirror (DM97-08; ALPAO, Montbonnot-Saint-Martin, France) placed at a pupil conjugate. Imaging and stimulation beams, traversing the system coaxially, were point-scanned across the retina, spanning a square field of 0.85×0.85 degrees of visual angle. The reflected IR light from the retina was sampled by a field-programmable gate array board (ML506; Xilinx, San Jose, CA, USA), producing video frames with 512×512 pixels (spatial resolution, 0.1 arcmin of visual angle per pixel) at ~ 30 Hz. Longitudinal chromatic aberration was compensated by a static relative vergence difference of 1 diopter (D) between the 840-nm and 543-nm light channels⁴⁸ and an individual adjustment of defocus of the deformable mirror for each eye, prioritizing focus in the stimulation channel. Transverse chromatic offsets were compensated dynamically with every stimulus presentation based on Purkinje-based pupil monitoring.^{46,49} The same system was used to monitor the diameter and position of the pupil relative to the light beam, ensuring that all light entered the eye at all times. Stimulus intensity was controlled via two cascaded acousto-optic modulators (AOMs; TEM-250-50-10-2FP with high extinction option; Brimrose, Sparks Glencoe, MD, USA).⁴⁵

PRL Determination

The PRL of fixation was determined by recording the exact retinal location at which a small (1.6×1.6 arcmin nominal size), flashing (3 Hz) visual stimulus landed during attempted fixation for 10 seconds in three individual AOSLO videos. Retinal fixation locations were then found by (1) automatically registering each frame strip-by-strip to a common reference frame of a single video,⁵⁰ (2) manual deletion of incorrectly registered frames (usually due to microsaccades, insufficient image quality, or eye blinks), and (3) tabulating all stimulus locations within the remaining co-registered frames (Fig. 1A). The final PRL estimate for each eye was the median stimulus location across three videos, equaling on average 387 frames (Fig. 1B). This location was defined as 0° eccentricity, or the PRL.

Cone Density Maps and Cone Density Centroid

Continuous maps of cone photoreceptor density were generated with imaging wavelengths of 543 nm (P1 and P2) or 788 nm (P3 and P4), similar to the PRL determination method. In the summed and normalized images, one human grader marked the location of each cone, assisted by convolutional neural network custom software.^{51,52} The Voronoi function of MATLAB (voronoiDiagram; MathWorks, Natick, MA, USA) was used to compute the area of each cone. Cone density was then calculated pixelwise by first identifying the nearest 150 cones around each pixel in the image and dividing the number of cones by their summed area. The cone density centroid (CDC) was the retinal location found as the weighted centroid of the area containing the highest 20% cone density values.⁹

Determination of Cone OS Length

Spectral-domain optical coherence tomography (OCT) images were acquired for all four participants in a $5^\circ \times 15^\circ$

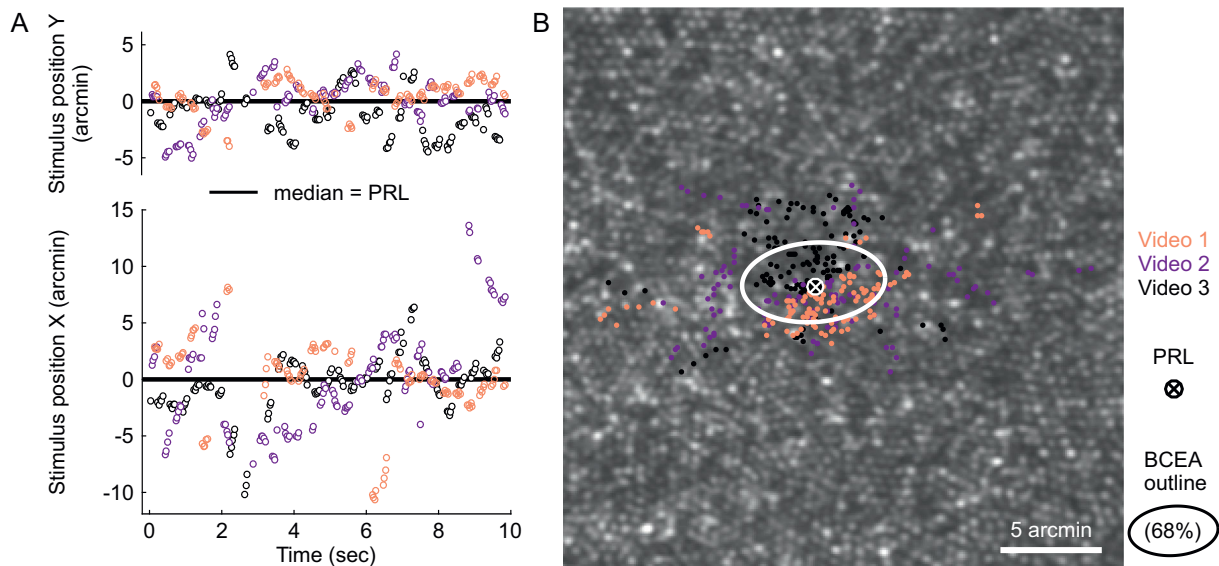


FIGURE 1. PRL determination from three 10-second videos. **(A)** The nominal fixation target was a 1.6×1.6 -arcmin square presented at a fixed position in the center of the AOSLO raster, flashing at 3 Hz. High-resolution eye motion traces were recorded in three 10-second epochs, tracking the position of the center of the target in retinal coordinates. Single dots represent frame-by-frame-derived retinal coordinates of the target, and colors indicate repeats. **(B)** Stimulus positions in relationship to the foveal cone photoreceptor mosaic. The bivariate contour ellipse was set to contain 68% of all stimulus locations. The participant's PRL (white ellipse and marker) was computed as the median data point, pooling all locations of the three consecutively recorded videos.

field, centered on the fovea with a B-scan spacing of $11\text{ }\mu\text{m}$ (Spectralis HRA+OCT; Heidelberg Engineering, Heidelberg, Germany). For further processing, the central 45 B-scans around the foveal pit were selected. Cone OS length was defined as the linear space between visible bands 2 and 3 in each B-scan, thought to correspond to the space between the ellipsoid zone and the interdigitation zone, respectively.⁵³ In a first step, these two bands were segmented using a brightness-based detection algorithm (Fig. 5A). Because the retinal pigment epithelium is thought to have a relatively uniform thickness and flat layout, a two-dimensional area fit across all B-scans for the third band was computed, reducing artifacts of the individual band marking. The width of both bands was modeled with a one-dimensional Gaussian profile, centered on the band marking. The OS length was defined as the linear space between the steepest parts of the declining slope of the second band and the rising slope of the third band.⁵³ These two-dimensional (2D) maps of OS length were registered with retinal AOSLO images by centering their maximal value at the CDC, assuming that both maps had a common center. Additionally, the limits of the sensitivity correlations were determined empirically by introducing a systematic offset in these maps. The location yielding the optimal correlation of thresholds, and OS length was marked in the OS maps as the OS offset (OSO) (Fig. 5B).

Increment Sensitivity Thresholds

With the PRL as a spatial anchor at the center of the test locations, 16 additional test locations were selected manually, close to the intersections of two concentric perimeters (spaced 6 and 12 arcmin) around the PRL with the horizontal, vertical, and diagonal meridians (Figs. 2A, 2B). At each of the 17 test locations, sensitivity thresholds were determined as the median of three to five repeat measurements per location. Sensitivity thresholds were estimated with QUEST.⁵⁴

Thresholds reflect incremental sensitivity due to stimulus presentation against the visible IR imaging raster background (about 5 cd/m^2 photopic luminance).^{42,55} Considering a residual defocus of 0.03 D ,⁵⁶ the stimulus edge length given by the full width at half maximum was about 0.8 arcmin, equaling between 1.5 (P1) and 1.8 (P4) times the diameter of the smallest cones. Threshold estimation was completed after 12 trials if the standard deviation (SD) value of QUEST was less or equal to $0.10\log$ arbitrary AOM voltage drive units (Fig. 2D). If the SD was higher at trial 12, the run was extended by additional trials until the SD criterion was met. The run was terminated and had to be repeated if the SD criterion was not met after 18 trials.

Real-time image stabilization enabled retinal tracking and repeated stimulation of the targeted test sites with an accuracy of about ± 1 foveolar cone diameter.⁵⁰ The exact stimulus location was marked during the trial delivery by a digital marker in an individual trial video. For each participant, a high signal-to-noise ratio image (sumframe) was created by summing all stimulus delivery frames across the experiment and by dividing by the numbers of frames contributing to each pixel. During the subsequent offline analysis, all stimulus delivery locations were automatically retrieved from the trial videos and registered via cross-correlation to the sumframe to create the target location map. Trials with suboptimal delivery (>0.6 arcmin deviance from median delivery location) were excluded from further analysis.

Due to small fixation eye motions during the experiments and a stationary AOSLO beam, stimuli were presented at variable locations within the IR imaging raster. The imaging raster, being the visible background during stimulation, had a non-uniform brightness along its horizontal axis due to the sinusoidal scanning velocity of the AOSLO. To compensate for this non-uniform background and to keep the visible contrast between stimulus and background constant, individual trial intensity was corrected based on its horizon-

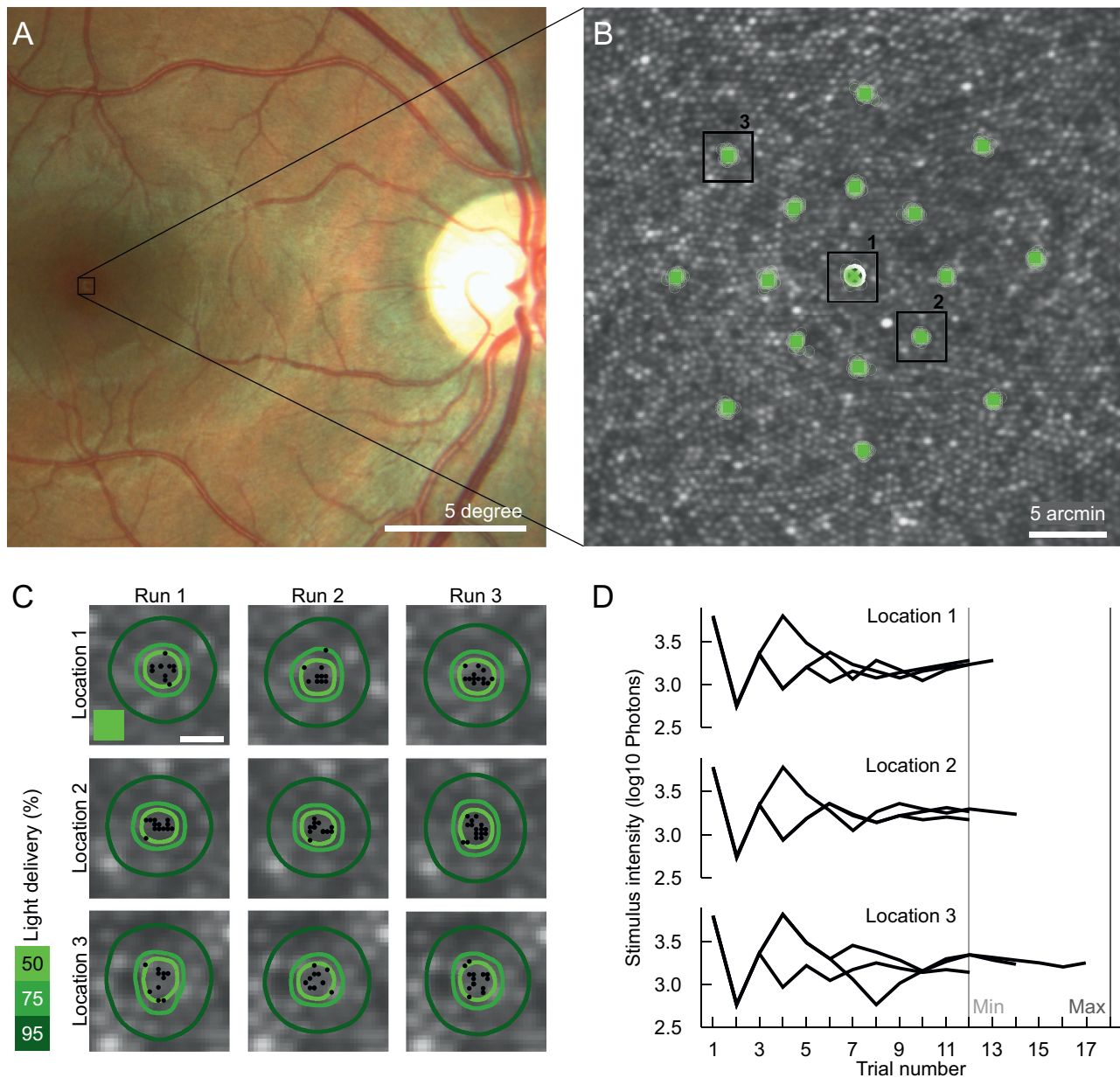


FIGURE 2. AOSLO-based microstimulation. **(A)** Color fundus image of one participant. The gray square shows the size and position of the AOSLO imaging and stimulation raster on the retina, positioned at the center of the fovea. **(B)** Cropped view of an averaged frame showing the AOSLO image of the central fovea. Retinal stimulation sites are marked by transparent green markers, and three sites are highlighted by black boxes to be further analyzed in the next panels. **(C)** Zoomed-in view of selected target sites. Markers indicate individual stimulus locations during repeated stimulation for threshold estimation. The green square represents the stimulus in raster pixel size. The contour lines mark 50%, 75%, and 95% of the summed light delivery for each run. Scale bar: 1 arcmin. **(D)** Exemplary progression of stimulus intensity based on the current threshold estimation via QUEST with three runs per test site. The individual run was completed when the standard deviation of the estimated threshold was ≤ 0.10 , resulting in a varying number of trials per test site and run.

tal position in the raster. In the stimulus-generating software, we opted to render stimuli with constant energy (not size), resulting in compensation factors ranging between 0.95 and 1.00. After trial rejection (about 5% due to imperfect registration and 1% due to an inaccurate delivery) and intensity correction, QUEST was rerun to compute the final threshold estimate. Trial deletions caused by stabilization errors produced higher QUEST SDs. Thresholds with SDs higher than 0.15 log arbitrary units (prioritizing data acquisition at this point) were excluded from the following analysis.

Conversion of Arbitrary Power Units to Number of Photons at the Cornea

Before and after each experimental run, maximal output power of the AOSLO stimulation light channel was measured at maximal AOM drive voltage with a silicon photodiode and power meter (S130C and PM320E; Thorlabs GmbH, Bergkirchen, Germany) in the transmitted portion of the stimulation beam after a 90/10 (T/R) beam splitter was placed in the light delivery arm of the AOSLO. The average of these two measurements was used for actual stimulus

power calculation of a given run. Typically, laser power fluctuated by less than 1% between measurements. With this, the QUEST threshold estimate (ThreshEst), thus far given in log₁₀ arbitrary AOM drive units, could be converted into a number of photons at the cornea using the following equation:

$$\text{Photons}_{\text{Thresh.}} = \frac{P_{\text{Max}} \cdot \text{Trans}_{\text{AOSLO}}}{E_{\text{Photon}}} \cdot t_{\text{Stim}} \cdot 10^{\text{ThreshEst.}}$$

where P_{Max} is the maximal AOM output power measured, $\text{Trans}_{\text{AOSLO}}$ is the relationship of maximal power fed into the AOSLO and the power detected at the eye's pupil position (about 0.065), t_{Stim} is the stimulus duration during a single presentation (2.45 μs), and E_{Photon} is the energy of a single photon.

Cone Light Capture Model and Image Systems Engineering Toolbox for Biology

To compute light catch in the targeted cones, a custom two-dimensional model of light acceptance was implemented in MATLAB. First, the sumframe of the target location map was registered via crosscorrelation⁵⁷ to a high signal-to-noise image of the foveal center used to create the cone location map. Second, cone center locations were used to compute a complete Voronoi tessellation of the mosaic defining the inner segment area of the individual cones. Third, the absorption characteristic across the inner segment area was modeled by a 2D Gaussian with a sigma value creating an aperture of 0.48 of the equivalent diameter.⁵⁸ The retinal stimulus was the result of a convolution of the nominal 7 × 7 AOSLO raster pixel stimulus and a diffraction-limited point spread function with a residual defocus of 0.03 D.⁵⁹ Finally, the convolved stimulus was multiplied by the cone absorption matrix to arrive at the amount of stimulus light absorbed by each cone. The reported value of percent of light per cone is based on the total light distribution given by the convolved stimulus matrix.

To independently model the impact of the biophysical properties of the cones, such as cone diameter, OS length, and cone class, on sensitivity thresholds, the Image Systems Engineering Toolbox for Biology (ISETBio) for MATLAB^{59,60} was used. In brief, ISETBio renders an ideal observer and its

theoretical response during a visual psychophysics experiment. Here, we employed subsets of ISETBio to simulate the retinal image during stimulation and the emerging photoreceptor response. The following parameters were used: The scene was a 511 × 511-pixel image with the central 7 × 7 pixels containing the stimulus. The field of view was set to 0.85°, and the background luminance set to 0.1 cd/m². The wavefront was set to be diffraction limited, with a varying residual defocus of 0.01, 0.03, and 0.05 D and zero longitudinal chromatic aberration. The hexagonal mosaic function was used with custom cone spacing and optical density. The optical density was calculated as the product of the OS length and an average absorbance of 0.014 μm⁻¹.⁶¹ Cone responses to each condition (varying cone density, optical density, and both coupled) were computed 10 times to account for simulated neural noise. Stimulus locations were shifted in steps of 0.6 arcsec (oversampling the AOSLO stimulus raster 10-fold). The cone class composition of the test site was controlled by adjusting the L- and M-cone spatial density parameter for each cone class and carefully checking the center surround configuration of the generated mosaic. These two simulations were both run with a residual defocus of 0.03 D and were repeated 33 times per condition.

RESULTS

Retinal Topography and the PRL

The PRL was found to be offset on average by 3 arcmin from the CDC (Fig. 3A). For each participant, the offset and the angle were different, ranging from 1 arcmin and 15° (P1) to 3 arcmin and 178° (P4), with a good repeatability of about 1 arcmin. The bivariate contour ellipse areas, indicating fixation stability, were found to be small in all participants (50, 67, 16, 30 arcmin², P1-4).

The foveal mosaics of all four observers could be fully resolved and marked to create continuous maps of cone density. Participants P1 to P4 were numbered according to their peak cone density values (13733, 15230, 18023, and 18406 cones/deg², respectively). Cone density dropped rapidly with increasing eccentricity (Fig. 4), on average to 67% of the peak cone density at a distance of about 20 arcmin from the CDC. The two-dimensional maps of cone OS length were found to show a similar topography as cone

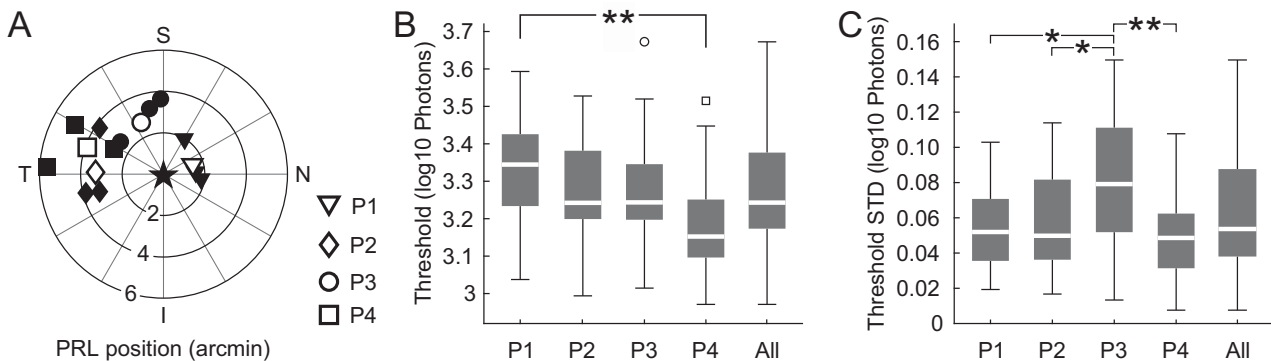


FIGURE 3. Fixation behavior and foveal increment sensitivity. (A) The PRL of each participant (P1–P4) is plotted relative to the location of the CDC (plot origin, star). Filled markers represent single measurements, and open markers are the final PRL based on three repeat measurements. Letters indicate nasal, temporal, inferior, and superior. (B) Pooled sensitivity thresholds across all test sites for each participant separately (P1–P4) and combined (“All”). Although the range (~0.5 log₁₀ units, whiskers), as well as the highest and lowest thresholds, were very similar across participants, the median, the first and third quartiles differed. (C) The observed standard deviations of repeated threshold estimations at the same test site were similar for three participants. Variability for P3 was higher than for the other three participants; 85% of all observed SDs were ≤0.10 log₁₀ photons.

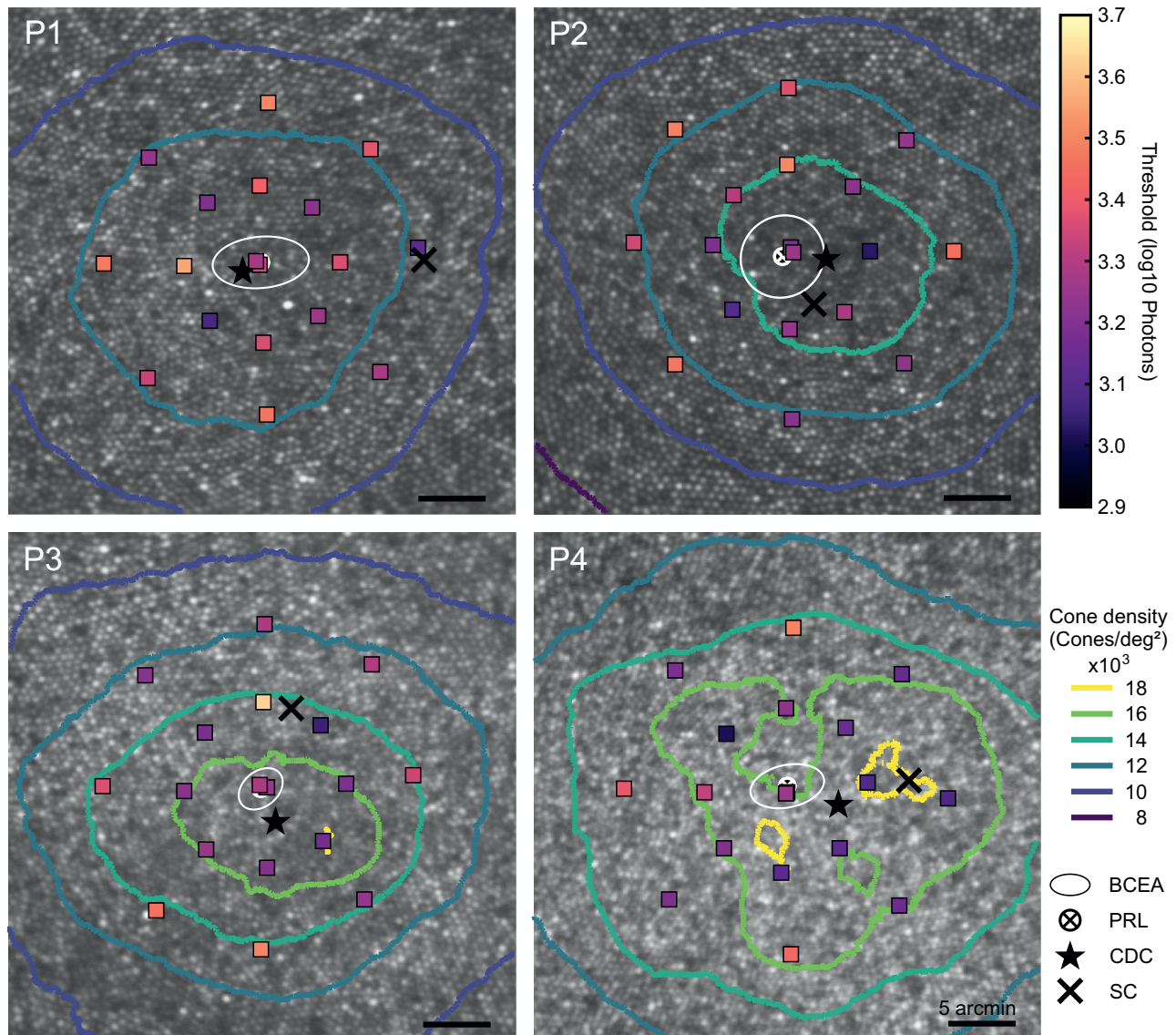


FIGURE 4. Sensitivity in relationship to cone topography and fixation behavior in all participants. Squares mark the average stimulus location for each test site, and coloring reflects the median sensitivity threshold in log10 photons. Marker area is four times the actual stimulus area on the retina and equals the average 95% outline of the summed light delivery (Fig. 1C). Cone density is indicated by colored contour lines. The PRL (white circle and crosshair), the location of the CDC (star), and an estimated location of the sensitivity centroid (SC, cross) are shown, as well.

density in each eye (Fig. 5). P1, the participant with the lowest peak cone density, also had the lowest maximal OS length (28 µm). For P2, P3, and P4, the maximal OS lengths were 32, 33, and 40 µm, respectively. Within the central 12-arcmin radius around the CDC, OS length ranges were 3, 4, and 8 µm (P1–P4, respectively).

Small Spot Sensitivity

Small spot sensitivity thresholds across participants were between 2.97 and 3.67 log10 photons at the cornea (median, 3.25 log10 photons). Although the range of thresholds across the four participants was similar (0.55, 0.54, 0.65, and 0.54 log10 photons for P1–P4, respectively) (Fig. 3B), their median thresholds decreased continuously from P1 to P4 (3.35, 3.24, 3.24, and 3.15 log10 photons, respectively). The thresholds observed in P1 were significantly higher

compared with the thresholds of P4 ($n = 18$; $P = 0.009$, two-sample t -test). The repeatability for each test site, computed across three to five reruns, was high, with an average SD of 0.06 ± 0.03 log10 photons (Fig. 3C).

Correlation Between Retinal Structure and Function

As a first observation, none of the participants had their PRL at the target site with the lowest threshold (5.7, 6.5, 6.5, and 6.0 arcmin distance from PRL for P1–P4, respectively). The average distance between the test site with the lowest threshold and highest cone density was 7.3 arcmin. In P1 and P2, the CDC was closer to the target site with the lowest threshold than the PRL (CDC distances of 4.5, 3.3, 7.8, and 9.8 arcmin).

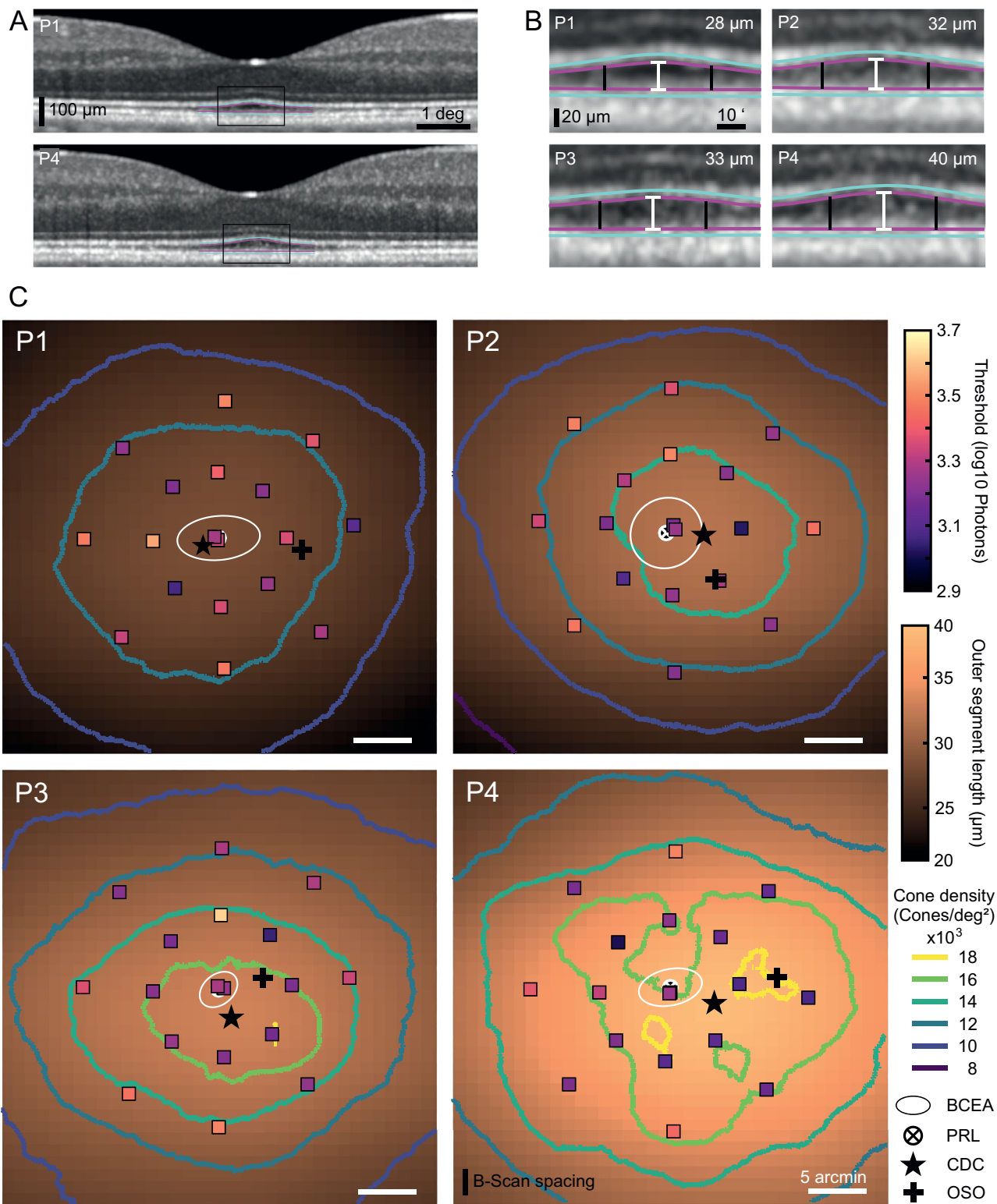


FIGURE 5. Cone OS length topography. (A) Foveal OCT B-scans from P1 and P4 and a zoomed-in view of the OS in the central fovea. (B) Further zoomed-in view of central OS and measurement demonstration for all four participants. The center of the band (cyan line) was semiautomatically marked. The OS start and end (magenta) were found by fitting a one-dimensional Gaussian centered on the second and third band. The estimated maximal OS length is stated in the upper right corner. (C) Interpolated 2D map of cone OS length in the central fovea for each participant. The OS map was centered on the CDC; the cross (OSO) marks an empirically determined center of the OS map relatively to the CDC and the test sites yielding the highest possible correlation between thresholds and OS length. The black vertical lines in B indicate the region of the 2D presentation in C.

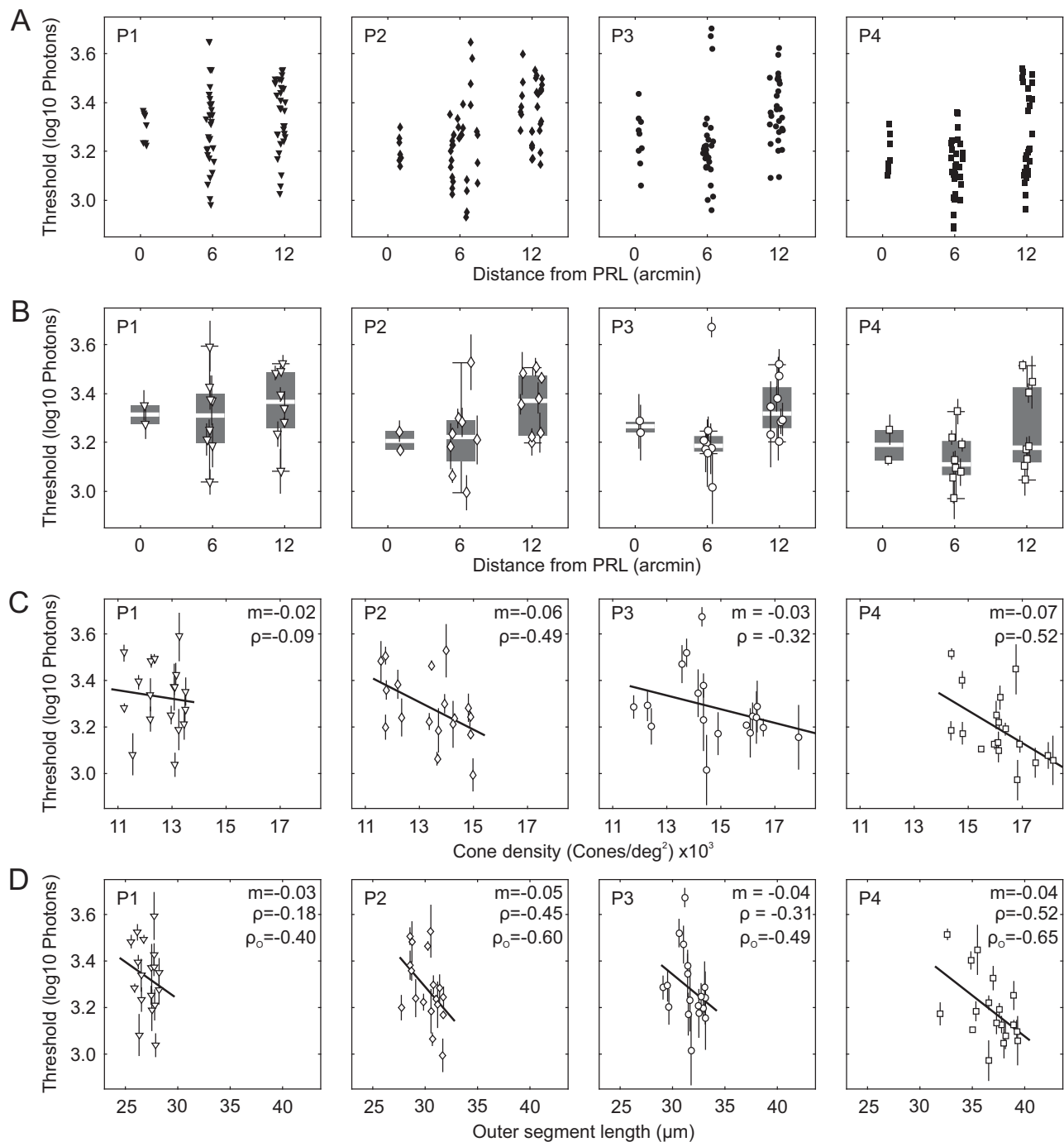


FIGURE 6. Sensitivity thresholds for each participant in relation to distance from PRL, cone density, and OS length. **(A)** Individual thresholds for the distance from the PRL for each test site are marked with *filled symbols*. **(B)** For each test site, we used the median threshold (*open symbols*) of repeated testing (3–5), and reported this value as the sensitivity of the test site. Boxplots show median (*white line*), first and third quartiles (*box*), and whiskers extending to 1.5-fold the distance between the first and third quartiles. **(C)** Median thresholds in relation to the cone density of the test site. **(D)** Median thresholds in relation to the OS length at the test site as obtained from the 2D map shown in Figure 5. The drawn correlation is based on the OS map centered on the CDC, and ρ_o is the optimal correlation based on OSO centering. Vertical lines in **B**, **C**, and **D** show the standard deviation across repeated runs, and thick black lines are linear fits to the data.

The range of cone densities at the test sites differed clearly within and among participants, with a difference from minimum to maximum of 2300 cones/deg² (11,215 to 13,198 cones/deg²) for P1, 3400 cones/deg² (12,564 to 14,971 cones/deg²) for P2, 6100 cones/deg² (11,786 to 17,881 cones/deg²) for P3, and 3800 cones/deg² (14,364

to 18,132 cones/deg²) for P4. Although the highest cone density of P4 was about one-third higher than the peak cone density of P1, sensitivity thresholds were similar at those locations. For further correlation analysis, the median threshold of repeated threshold estimations at the same test location was used (Figs. 6A, 6B).

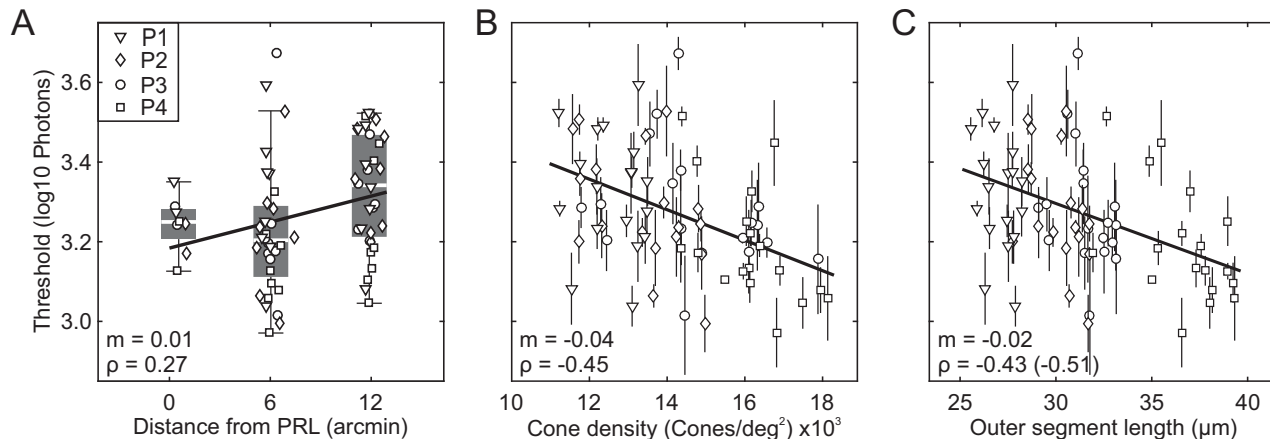


FIGURE 7. Pooling threshold data across participants. **(A)** Sensitivity thresholds of all participants as a function of test site distance from PRL, given as median (white line) and first and third quartiles (box). Whiskers extend to 1.5-fold the distance between the first and third quartiles. For the pooled data set, a bend toward lower thresholds at 6 arcmin was observed. **(B)** Thresholds as a function of local cone density at the test site. Vertical lines show the standard deviations of threshold estimates for repeated testing. Thresholds and cone densities showed a moderate correlation ($\rho = -0.45$). **(C)** Thresholds as a function of cone OS lengths showing a moderate correlation ($\rho = -0.43$). Using the OSO for all participants, the optimal correlation ρ_O was -0.51 . All independent variables (distance, density, OS length) were pairwise significantly correlated with each other ($P < 0.001$, data not shown).

In each participant, the lowest single threshold was observed 6 arcmin away from the PRL (Fig. 6B). Also, the median threshold at 6 arcmin distance was almost identical (P1 and P2) or even lower (P3 and P4) than the median threshold at the PRL. For the 12-arcmin eccentricity, we observed a similar or higher median threshold compared with the median PRL threshold. In P3 we observed an extremely high threshold at one location that was 0.3 log₁₀ photons higher than the second highest threshold.

Plotting the individual thresholds as a function of the cone density of the test site revealed a tendency toward lower thresholds for higher cone densities (Fig. 6C), with correlation coefficients of $\rho = -0.09$, -0.49 , -0.32 , and -0.52 for P1 to P4, respectively, with corresponding slopes of $m = -0.02$, -0.06 , -0.03 , and -0.07 log₁₀ photons per 10³ cones/deg² for P1 to P4, respectively.

As expected, correlating thresholds with foveal cone OS length revealed a similar trend: Thresholds were generally lower at sites with higher OS length (Fig. 6D). Correlation coefficients were $\rho = -0.18$, -0.45 , -0.31 , and -0.52 for P1 to P4, respectively. The slopes were almost the same across the four participants ($m = -0.03$, -0.05 , -0.04 , and -0.04 log₁₀ photons/μm for P1 to P4, respectively). Based on an empirical approach placing the OS map to maximize the correlation between OS length and thresholds yielded optimal correlation coefficients of $\rho_O = -0.40$, -0.60 , -0.49 , and -0.65 for P1 to P4, respectively. The corresponding optimized displacement of the OS length map relative to the CDC, the OS offset, is shown in Figure 5C.

When data were pooled across participants, the correlation between the thresholds and the distance from the PRL was given by a slope of 0.65 log₁₀ photons/deg ($\rho = 0.27$) (Fig. 7A). The observed decrease of thresholds at 6 arcmin distance from the PRL remained in the combined dataset. Thresholds as a function of cone density had a negative slope of -0.04 log₁₀ photons per 10³ cones/deg² ($\rho = -0.45$) (Fig. 7B). The correlation between thresholds and OS length indicated an average decrease of thresholds of -0.02 log₁₀ photons/μm in the pooled dataset ($\rho = -0.43$) (Fig. 7C).

Modeling the Impact of Cone Density, OS Length, and Distance From PRL on Sensitivity

Because the individual factors of cone density, OS length, and distance from PRL were all highly significantly correlated with each other ($P < 0.001$; data not shown), a physiological model of cone light capture (ISETBio) was employed to model the impact of these three factors independently. The first hypothesis tested with ISETBio modeling was whether the correlation between detection thresholds and cone density could be caused by spatial summation effects, as the stimulus light diameter was about 1.5 times the average foveal cone diameter. Therefore, the average distance to the surrounding neighbors could have played an important role. Using the cone spacing according to the observed cone densities, the results from this model were best described by a linear regression with a slope of about -0.01 log₁₀ photons per 10³ cones/deg², roughly four times lower than the observation in our data (Fig. 8A). ISETBio was also used to test the influence of OS length and associated optical density on sensitivity and predicted a strong impact of OS length on thresholds ($\rho = -0.99$), with a slope of -0.008 log₁₀ photons/μm OS length based on the observed OS lengths (Fig. 8B).

In the following step, the slopes derived for 0.03 D residual defocus⁵⁶ were used to remove the estimated proportional influence of cone density and OS length from the observed thresholds. The rescaled thresholds were supposed to vary only due to retinal eccentricity in terms of distance from the PRL (Fig. 8C). When all rescaled thresholds were plotted as a function of distance to the PRL, a linear fit with a slope of 0.01 log₁₀ photons/arcmin PRL distance ($\rho = 0.21$) emerged.

These rescaled thresholds were also used to compute the location of the sensitivity centroid (SC) for each participant by finding the retinal coordinate yielding the highest value of ρ for corrected thresholds against distance from this coordinate (Fig. 3). The SC was offset from the PRL (11.7, 3.8, 4.8, and 7.5 arcmin distance) or CDC (13.1, 2.2, 6.8, and 3.7 arcmin distance) in all participants.

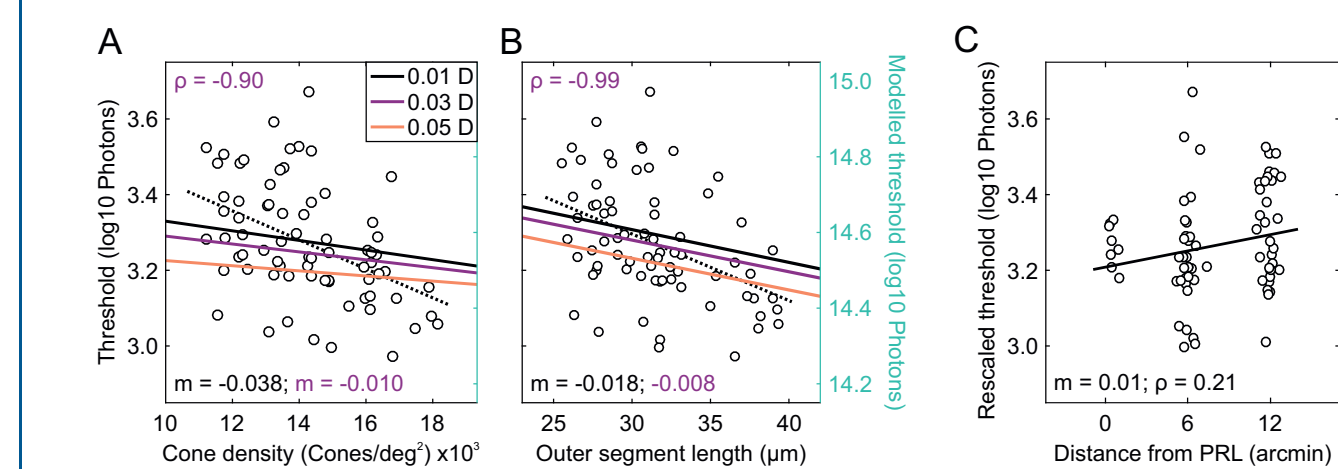


FIGURE 8. ISETBio model testing the impact of cone density and OS length. (A) The ISETBio model evaluated the threshold photons to elicit a certain number of isomerizations, fitted for 0.01 D, 0.03 D, and 0.05 D residual defocus. The simulation revealed only a small influence of cone density and therefore spacing on sensitivity thresholds ($m = -0.010$ and $\rho = -0.90$ with 0.03 D), too small to explain the observations. (B) To test the influence of OS length and therefore optical density on sensitivity, we fed the observed range of OS lengths (25–40 μm) in our ISETBio model, which predicted a strong impact of different OS lengths on thresholds ($m = -0.008$ and $\rho = -0.99$ with 0.03 D). (C) The pooled data of the rescaled thresholds, from which the OS length and density influence was removed (see Methods), against the distance from the participant's PRL (Fig. 4). The dotted line in A and B represent the linear regression introduced in Figure 7.

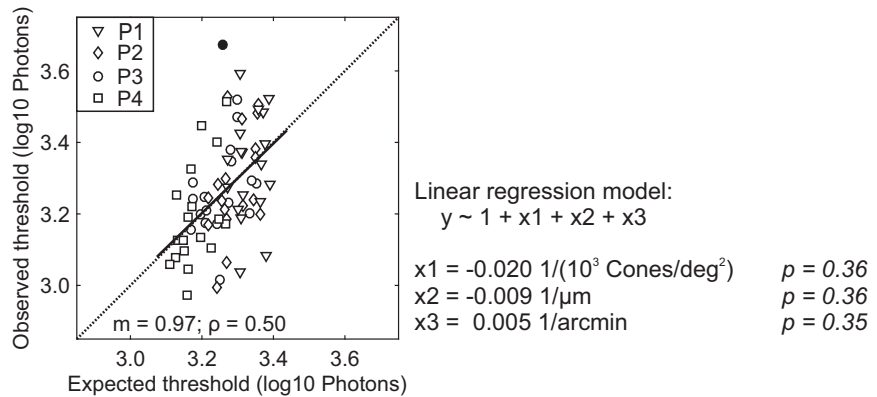


FIGURE 9. Estimating sensitivity thresholds from retinal factors. The expected threshold was derived from the cone density, OS length, and distance from the PRL of the test site (Fig. 4) using a linear regression model with the given function. The solid line is the linear fit to the data ($m = 0.97$, $\rho = 0.50$), and the dotted line shows the 1:1 relationship. Slopes and P values for each parameter are stated. The single threshold marked by the filled symbol was ignored in this analysis due to its uncertain nature.

Finally, we used a linear model (fitlm, MATLAB) to estimate the individual influence of the three factors tested here (cone density, OS length and PRL distance of the test site) on sensitivity thresholds (Fig. 9). The slopes of the individual factors were given by $-0.020 \log_{10}$ photons per 10^3 cones/deg², $-0.009 \log_{10}$ photons/μm, and $0.005 \log_{10}$ photons/arcmin PRL distance. All three factors had the same impact on the sensitivity thresholds, based on P values of about 0.36 for cone density and OS length and 0.35 for PRL distance. In combination, the estimated thresholds were best fitted by a linear regression with a slope of 0.97 ($\rho = 0.50$).

Modeling the Impact of Stimulus Position and Cone Class Composition

Given a residual variability of $\pm 0.20 \log_{10}$ photons from the prediction, we also looked at the variability that could

possibly be due to the exact stimulus position on the cone mosaic. To test the hypothesis that the exact placement of the test stimulus relative to the cone mosaic affects sensitivity at that site, the photon catch of each cone for the average stimulus location during each run was modeled. An example is shown in Figure 10A for two different cases. The first case shows two different target sites in the retina of P2. At both target sites, the exact stimulus locations on the cone mosaic were similar, but the thresholds differed significantly by $0.36 \log_{10}$ photons ($P = 0.03$, Mann–Whitney U test; $n = 4$). In the second example from P4, the stimulus placement differed; the first one was centered on a single cone, and the second one was placed in the middle of three cones. For this case, we found similar sensitivity thresholds, with a non-significant difference ($P = 0.49$, Mann–Whitney U-test; $n = 4$). When all thresholds were plotted against light catch in the nearest cone, no significant correlation emerged (Fig. 10B). The ISETBio model, by creating a generalized perfect

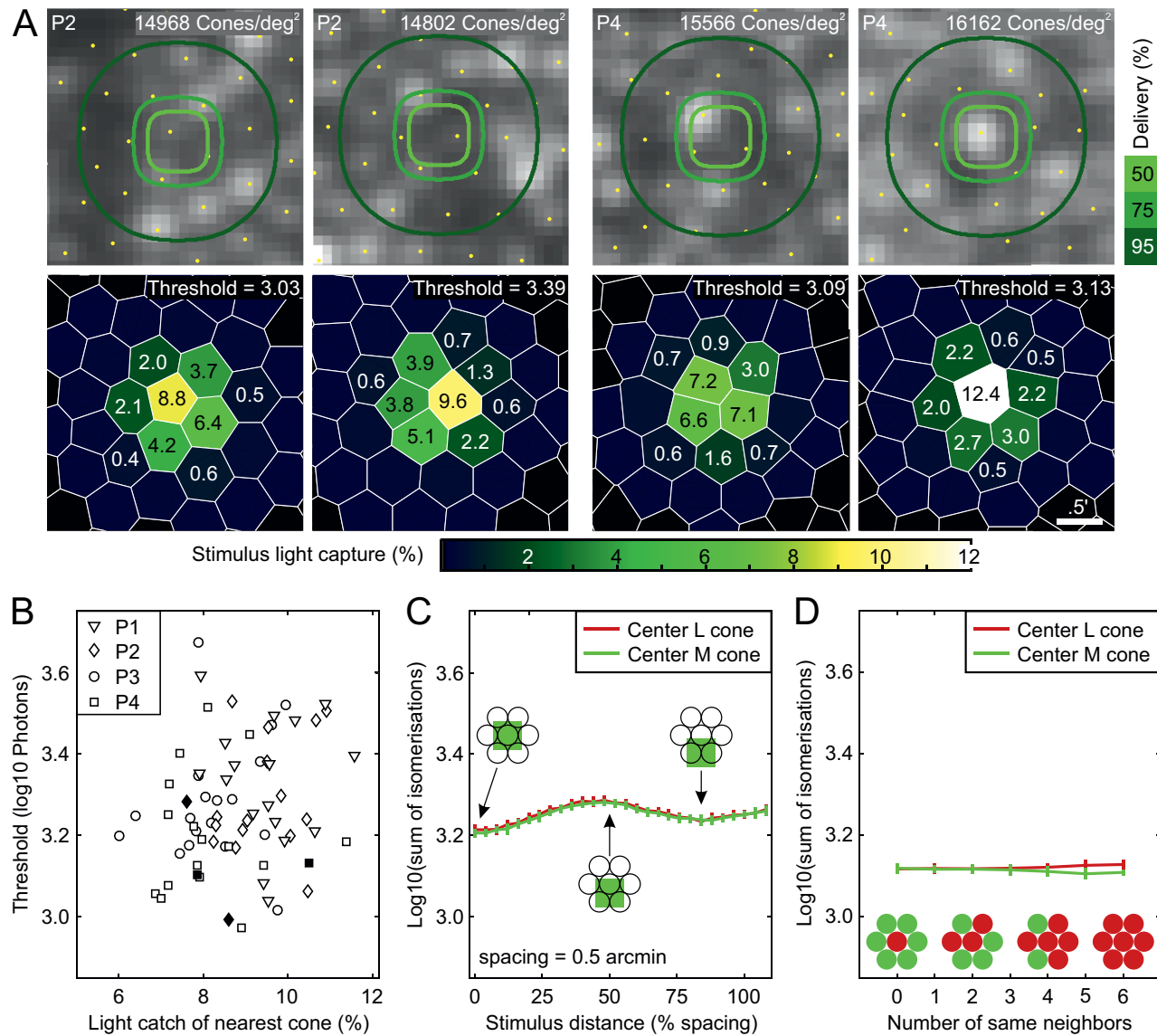


FIGURE 10. Possible sources of threshold variability. (A) We used the cone maps to model the light catch for each cone at the target site. The left two panels show two different test sites of P2, with a similar light catch situation. The observed thresholds for these test sites differed significantly ($P = 0.03$, Mann–Whitney U test; $n = 4$). The right two panels show two different test sites of P4, with different light catch situations. In the first condition, three cones are supposed to catch the same number of photons, whereas in the second condition the major portion of stimulus photons are being caught by a single cone. The observed thresholds for these test sites differ insignificantly ($P = 0.49$, Mann–Whitney U test; $n = 4$). (B) The data pooled across all participants. Small light catch numbers indicate a three-cone position, and high numbers a single-cone center position. Example datasets shown in A are highlighted with filled symbols. There was no significant correlation between observed thresholds and stimulus delivery condition. (C) This observation was confirmed by an ISETBio model testing the influence of stimulus position on the number of isomerizations. The model showed a maximal change of $0.1 \log_{10}$ isomerizations for different stimulus positions. (D) The ISETBio model tested the influence of different cone class compositions at the test site. This model does not contain any inter-cone class inhibition and therefore shows that only a slight increase of isomerizations if solely L-cones were activated. The error bars in C and D indicate the ISETBio simulated retinal noise.

hexagonal retinal mosaic, supported this observation: When shifting the stimulus systematically from a cone-centered position to a position in the middle between cones, the number of isomerizations changed by $0.1 \log_{10}$ space (**Fig. 10C**). There was no difference if the center cone was an L- or M-cone. Such small changes could not explain the observed variability of $\pm 0.3 \log_{10}$ photons but could be one reason for the observed intra-run variability of $0.06 \log_{10}$ photons due to small stimulus displacements

caused by residual errors of the real-time stabilization (**Fig. 2C**).

Another reason for such variability could be the composition of cone classes at the stimulus location. Based on ISETBio, the maximal difference was $0.02 \log_{10}$ isomerizations for a stimulus location consisting of only L-cones versus only M-cones (**Fig. 10D**). This model did not contain any specific L/M-cone interactions and only used cone class-specific spectral sensitivity.

DISCUSSION

We studied the anatomical and functional profile of the center of the foveola of four human participants with adaptive optics-assisted *in vivo* imaging and microstimulation to quantify the impact of three key morphological factors on visual sensitivity with cellular resolution.

Distance From PRL

Apart from the observation that the PRL is offset from the cone topography center mirror symmetrically between fellow eyes,⁹ there is currently no other structural indication for why it forms where it does.^{26,39,40} Our hypothesis was that the PRL forms at a location with peak visual sensitivity. However, we found a rather plateau-like sensitivity profile within the central 6-arcmin radius around the PRL with reduced sensitivity at about 12-arcmin eccentricity, resulting in a much flatter slope than the anatomical topography of cone density and OS length changes in the same region. In all eyes, the location of the individual peak sensitivity, as well as the empirically determined SC, was offset from the PRL (Figs. 3, 5). The distance between the PRL and the SC was small, about 7 arcmin on average, and the average thresholds at the PRL and 6-arcmin eccentricity were similar. Therefore, sensitivity can be ruled out as a major driving factor of the PRL formation. A recent study from our group found a systematical offset between the PRL and the CDC favoring binocular fixation as a more important factor for the location of the PRL.⁹

Cone Density

We observed a correlation between median sensitivity and the participant's peak cone density (PCD), a finding supported by recent clinical work in pathological retinas.^{16–18,62,63} When sensitivity was correlated with eccentricity (and thus cone density), it was shown that a small stimulus size, equal to or lower than the according spatial summation area, is crucial to resolve the foveal sensitivity peak.^{11,64,65} Our stimulus (about 1-arcmin full width at half maximum diameter) met this criterion because the spatial summation area of the foveola was found to be about 2.5 arcmin in diameter.²¹ That spatial summation is at play in our data can be concluded by considering the estimated number of isomerizations at threshold: Given that the overall transmission for 543 nm light is 43% (neglecting individual and age-related variations),⁶⁶ the average detection threshold was 2.9 log₁₀ photons at the cone inner segments. The two-dimensional model of cone capture showed that the central cones at the target site catch between 55 photons (7% of the stimulus light on the retina) and 95 photons (12%) at threshold. With an optical density of about 0.5,⁶⁷ this corresponds to 27 or 45 isomerizations in either L- or M-cones. This is close to the estimated number of isomerizations (about 22–71) at the absolute cone threshold,⁶⁸ which would indicate complete adaptation to the IR background in our stimulus situation. The 840-nm imaging light had a radiant power of about 14.8 log₁₀ photons/s at the cornea (170 μW). With an overall ocular transmission factor of 0.55 for 840 nm⁶⁶ and a field size of 0.85°, the estimated photon rate at an individual inner segment was 10.7 log₁₀ photons/s. If a fraction of 33% was transferred into the OSs (using a Gaussian absorption model⁵⁸ and assuming a cone integration time [cit] of 100 ms,^{69,70} we yielded roughly 250 R*/cit per

L-cone and 22 R*/cit per M-cone. Thus, the observed increment thresholds followed Weber's law⁷¹ only for L-cones. In other words, based on differential cone isomerizations induced by the background light, a threshold variability of about 1 log unit would have been expected. However, this was not observed in our data, and we conclude that a cone-class-encompassing summation mechanism seems likely.

Modeling of light propagation in cone inner and outer segments revealed that a smaller cone aperture is beneficial for increased quantum catch due to the waveguiding properties of the cone.⁵⁶

As a consequence, a sharp peak of sensitivity within the foveola, centered on the highest cone density, would have been expected, based on the steep increase in the dendritic field size of the parasol ganglion cell⁷² and the inner segment diameter of the cone.^{5,73} In recent microperimetry studies using a 6-arcmin stimulus diameter, a sensitivity decline with a slope of about 1.4-dB/deg eccentricity was found.^{11,65,74} In our study, using a stimulus smaller than Ricco's area, we observed a four-times steeper slope of about 6 dB/deg within the central 0.2°, but with a sensitivity plateau for the central 0.1° radius, which may reflect the topography of parasol dendritic field sizes. Biophysical modeling predicted only a small influence of cone spacing on sensitivity due to the size of our stimulus, without taking into account effects that are due to different light propagation in differently sized cones⁵⁶ or increased summation due to an increased dendritic field size of ganglion cells.⁷²

OS Length

Following the approach suggested by Spaide and Curcio,⁵³ our peak OS lengths (average across participants, 33 μm) were shorter compared with reports for healthy participants from conventional OCT (with averages of ~41 μm,⁷⁵ ~47 μm,⁷⁶ and ~52 μm⁷⁷), but were closer to histological reports (with averages of 35 μm,⁷⁸ >45 μm,⁷⁹ and 30 μm⁸⁰). We found that sensitivity was moderately correlated with cone OS length within the steep topography of the foveola. In patients with inherited retinal degeneration, a relationship between visual sensitivity and OS length was recently observed by Foote et al.,¹⁸ but not by Bensinger et al.¹⁷ A significant correlation between OS length and sensitivity was furthermore reported in other cases of retinal diseases such as age-related macular degeneration,^{13,81} glaucoma,⁸² and retinitis pigmentosa.¹²

Given that the light-sensitive photopigment is accumulated in the photoreceptor OS and based on the assumption that the amount of photopigment per cone is relatively constant,⁶ OS length is directly linked to optical density.^{61,83} Furthermore, a correlated decrease of photopigment density and OS length with eccentricity was demonstrated.⁷ A biophysical model of the cone's quantum catch based on the optical density confirmed the observation that longer OSs are likely to absorb more photons and therefore convey increased sensitivity.

We report a strong correlation between maximal OS length and peak cone density, an observation shared by other groups to varying degrees.^{16–18,76,84} By computationally shifting the OS length map relative to cone density (OSO) (Fig. 5), the correlation between OS length and sensitivity changed only marginally, indicating that these two are indeed co-aligned.

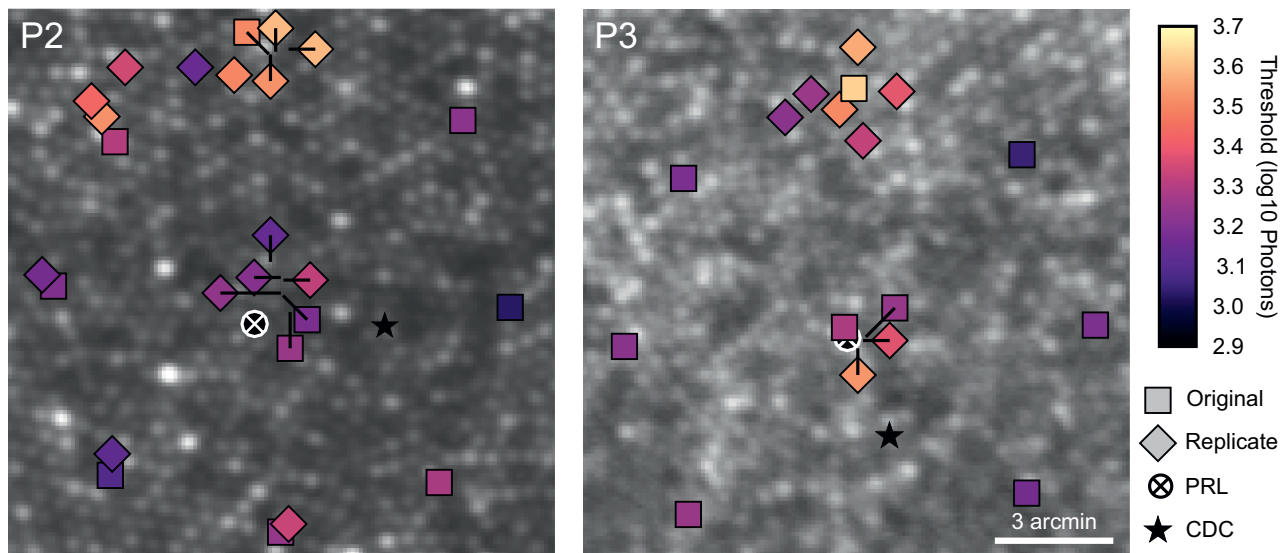


FIGURE 11. Replicate testing of test sites with conspicuous high thresholds. *Squares* mark the formerly shown original test sites (Fig. 4), and *diamonds* mark additionally collected data. The markers match the nominal size of the stimulus. To reduce overlapping, markers were shifted, and the tip of a *black line* indicates the center of the retinal location. For P2 the replicate data points were collected 2 days earlier during a piloting experiment. For P3, the additional locations were tested on the same day, due to the suspiciously high threshold. The PRL is marked with the *white circle* and *crosshair*, and the CDC is indicated by a *black star*.

Variability of Threshold Estimates

The impact of the above factors could explain visual sensitivity in the foveal center reasonably well ($\rho = 0.50$). The P value was similar for all three factors (about 0.36); thus, if two factors (e.g., eccentricity and OS length) are known, an estimation of foveal sensitivity could be derived. However, a threshold variability of $\pm 0.2 \log_{10}$ photons remained unexplained in the three-parameter model. Biophysical modeling ruled out light catch differences due to differing stimulus positions on the cone mosaic⁴² or the spectral identity of the cone at the test site as major sources for the observed variability (Fig. 10). Variations in the optical wave guidance characteristics, due, for example, to the photopigment density of the cone,⁸⁵ could not be tested here.

In replicate testing, demonstrating that cell-resolved sensitivity thresholds were stable across days, we observed a maximal threshold difference of 0.4 \log_{10} photons between test sites spaced only 1 arcmin apart, equaling four times the intra-run variability (Fig. 11). A similar observation was reported recently with cone-sized stimuli, where thresholds differed by up to 0.3 log units between neighboring cones.⁸⁶

Minimal variations of the photopigment spectral sensitivity are likely to occur in the same retina,^{87,88} and females specifically are extremely likely to have two spectrally different L-cones, even though functional tetrachromacy has not yet been observed.⁸⁹ Given the fact that the female participant (P2) did not show an increased cone–cone variability (Fig. 3C) and the ISETBio model predicted a neglectable influence of the cone class on thresholds (Fig. 10D), we assume that possible photopigment variations would not account for the high sensitivity differences between neighboring cones alone. Thus, post-receptoral retinal architecture has to be considered further. Individual cone inputs to ganglion cells vary due to functional weighting at the

cone bipolar or bipolar ganglion synapses.^{90–92} So far, in vitro studies have reported linear and nonlinear interactions between cones due to subunits within receptive fields of a ganglion cell.⁹³ The size and location of these subunits in the receptive field of the ganglion cell were reported to correspond directly to the bipolar cells.⁹⁴

Horizontal signal processing is realized by H1 and H2 horizontal cells. When an L- and M-cone are connected to the same horizontal cell, elevated activation of the L-cone that is due to the 840-nm imaging background would lead to an inhibition of the M-cone response to the stimulus.^{55,95} Neighboring S-cones were found to have a suppressing effect on thresholds.⁵⁵ The influence of S-cones in the central fovea has to be considered for the following reasons: First, histology showed that scattered S-cones can be found within the central 0.15°^{96,97} and, for individual cases, even within the foveola.⁹⁸ Second, it is likely that our pulsed light source (pulse durations of about 25 ps and a frequency of 100 MHz) activates S-cones via a two-photon effect of the infrared imaging light.⁹⁹ In the unlikely event of a stimulus being placed centered on an S-cone, the expected threshold would have been elevated by 0.3 \log_{10} photons, based on our simulation shown in Figure 10A. Therefore, the conspicuously high threshold found in P3 could be due to an S-cone situated at that location (Fig. 11).

In conclusion, we found that peak sensitivity does not coincide with the PRL. Small spot sensitivity within the foveola is influenced by the individual cellular morphology and distance from the PRL. On a cellular scale, we observed reproducible and significant threshold differences between neighboring cones *in vivo*, supporting *in vitro* reports of individual cone weights within receptive fields. In combination, these findings will be helpful in determining the parameters for normal cone function in AOSLO microstimulation testing and thus distinguishing between healthy and pathological cone function.

Acknowledgments

The authors thank Lawrence Sincich (University of Alabama, Birmingham, AL, USA) for helpful comments on a previous version of the manuscript, and Pavan Tiruveedhula (University of California, Berkeley, CA, USA) and Michael Linden for technical assistance.

Funded by the German Research Foundation (DFG, Ha5323/5-1) and the Carl Zeiss Förderfonds (HC-AOSLO).

Disclosure: **N. Domdei**, None; **J.L. Reiniger**, None; **F.G. Holz**, None; **W.M. Harmening**, None

References

1. Yuodelis C, Hendrickson A. A qualitative and quantitative analysis of the human fovea during development. *Vision Res.* 1986;26(6):847–855.
2. Zhang C, Kim YJ, Silverstein AR, et al. Circuit reorganization shapes the developing human foveal midget connectome toward single-cone resolution. *Neuron.* 2020;108(5):905–918.e3.
3. Provis JM, Dubis AM, Maddess T, Carroll J. Adaptation of the central retina for high acuity vision: cones, the fovea and the avascular zone. *Prog Retin Eye Res.* 2013;35:63–81.
4. Cuenca N, Ortúñoz-Lizarán I, Sánchez-Sáez X, et al. Interpretation of OCT and OCTA images from a histological approach: clinical and experimental implications. *Prog Retin Eye Res.* 2020;77:100828.
5. Curcio CA, Sloan KR, Kalina RE, Hendrickson AE. Human photoreceptor topography. *J Comp Neurol.* 1990;292(4):497–523.
6. Marcos S, Tornow RP, Elsner AE, Navarro R. Foveal cone spacing and cone photopigment density difference: Objective measurements in the same subjects. *Vision Res.* 1997;37(14):1909–1915.
7. Elsner AE, Burns SA, Webb RH. Mapping cone photopigment optical density. *J Opt Soc Am A.* 1993;10(1):52.
8. Wang Y, Bensaid N, Tiruveedhula P, Ma J, Ravikumar S, Roorda A. Human foveal cone photoreceptor topography and its dependence on eye length. *Elife.* 2019;8:e47148.
9. Reiniger JL, Domdei N, Holz FG, Harmening WM. Human gaze is systematically offset from the center of cone topography. *Curr Biol.* 2021;31:1–6, <https://doi.org/10.1016/j.cub.2021.07.005>.
10. Hecht S, Haig C, Wald G. The dark adaptation of retinal fields of different size and location. *J Gen Physiol.* 1935;19(2):321–337.
11. Choi AYJ, Nivison-Smith L, Khuu SK, Kalloniatis M. Determining spatial summation and its effect on contrast sensitivity across the central 20 degrees of visual field. *PLoS One.* 2016;11(7):e0158263.
12. Mitamura Y, Aizawa S, Baba T, Hagiwara A, Yamamoto S. Correlation between retinal sensitivity and photoreceptor inner/outer segment junction in patients with retinitis pigmentosa. *Br J Ophthalmol.* 2009;93(1):126–127.
13. Acton JH, Theodore Smith R, Hood DC, Greenstein VC. Relationship between retinal layer thickness and the visual field in early age-related macular degeneration. *Invest Ophthalmol Vis Sci.* 2012;53(12):7618–7624.
14. Chung HW, Yun CM, Kim JT, Kim SW, Oh J, Huh K. Retinal sensitivity assessed by microperimetry and corresponding retinal structure and thickness in resolved central serous chorioretinopathy. *Eye (Lond).* 2014;28(10):1223–1230.
15. Ratnam K, Carroll J, Porco TC, Duncan JL, Roorda A. Relationship between foveal cone structure and clinical measures of visual function in patients with inherited retinal degenerations. *Invest Ophthalmol Vis Sci.* 2013;54(8):5836–5847.
16. Foote KG, Loumou P, Griffin S, et al. Relationship between foveal cone structure and visual acuity measured with adaptive optics scanning laser ophthalmoscopy in retinal degeneration. *Invest Ophthalmol Vis Sci.* 2018;59(8):3385–3393.
17. Bensinger E, Rinella N, Saud A, et al. Loss of foveal cone structure precedes loss of visual acuity in patients with rod-cone degeneration. *Invest Ophthalmol Vis Sci.* 2019;60(8):3187–3196.
18. Foote KG, De la Huerta I, Gustafson K, et al. Cone spacing correlates with retinal thickness and microperimetry in patients with inherited retinal degenerations. *Invest Ophthalmol Vis Sci.* 2019;60(4):1234–1243.
19. Takeshita D, Smeds L, Ala-Laurila P. Processing of single-photon responses in the mammalian on and off retinal pathways at the sensitivity limit of vision. *Philos Trans R Soc Lond B Biol Sci.* 2017;372(1717):20160073.
20. Volbrecht VJ, Shrago EE, Schefrin BE, Werner JS. Spatial summation in human cone mechanisms from 0 degrees to 20 degrees in the superior retina. *J Opt Soc Am A Opt Image Sci Vis.* 2000;17(3):641–650.
21. Tuten WS, Cooper RF, Tiruveedhula P, et al. Spatial summation in the human fovea: do normal optical aberrations and fixational eye movements have an effect? *J Vis.* 2018;18(8):6.
22. Goldberg ME, Walker MF. The control of gaze. In: Kandel ER, Schwartz JH, Jessell TM, Siegelbaum SA, Hudspeth AJ, eds. *Principles of Neural Science.* 5th ed. New York: McGraw-Hill; 2013:894–916.
23. Poletti M, Listorti C, Rucci M. Microscopic eye movements compensate for nonhomogeneous vision within the fovea. *Curr Biol.* 2013;23(17):1691–1695.
24. Nachmias J. Two-dimensional motion of the retinal image during monocular fixation. *J Opt Soc Am.* 1959;49(9):901–908.
25. Steinman RM. Effect of target size, luminance, and color on monocular fixation. *J Opt Soc Am.* 1965;55(9):1158.
26. Putnam NM, Hofer HJ, Doble N, Chen L, Carroll J, Williams DR. The locus of fixation and the foveal cone mosaic. *J Vis.* 2005;5(7):632–639.
27. Crossland MD, Engel SA, Legge GE. The preferred retinal locus in macular disease: toward a consensus definition. *Retina.* 2011;31(10):2109–2114.
28. von Noorden GK, Mackensen G. Phenomenology of eccentric fixation. *Am J Ophthalmol.* 1962;53(4):642–661.
29. Timberlake GT, Mainster MA, Peli E, Augliere RA, Essock EA, Arend LE. Reading with a macular scotoma. I. Retinal location of scotoma and fixation area. *Invest Ophthalmol Vis Sci.* 1986;27(7):1137–1147.
30. Timberlake GT, Peli E, Essock EA, Augliere RA. Reading with a macular scotoma. II. Retinal locus for scanning text. *Invest Ophthalmol Vis Sci.* 1987;28(8):1268–1274.
31. Whittaker SG, Budd J, Cummings RW. Eccentric fixation with macular scotoma. *Invest Ophthalmol Vis Sci.* 1988;29(2):268–278.
32. Crossland MD, Culham LE, Kabanarou SA, Rubin GS. Preferred retinal locus development in patients with macular disease. *Ophthalmology.* 2005;112(9):1579–1585.
33. Rees AL, Kabanarou SA, Culham LE, Rubin G. Can retinal eccentricity predict visual acuity and contrast sensitivity at the PRL in AMD patients? *Int Congr Ser.* 2005;1282:694–698.
34. Barlow HB. Eye movements during fixation. *J Physiol.* 1952;116:290–306.
35. Cornsweet TN. Determination of the stimuli for involuntary drifts and saccadic eye movements. *J Opt Soc Am.* 1956;46(11):987–993.
36. Wilk MA, Dubis AM, Cooper RF, Summerfelt P, Dubra A, Carroll J. Assessing the spatial relationship between fixation and foveal specializations. *Vision Res.* 2017;132:53–61.

37. Bedell HE. A functional test of foveal fixation based upon differential cone directional sensitivity. *Vision Res.* 1980;20(6):557–560.
38. Zeffren BS, Applegate RA, Bradley A, van Heuven WA. Retinal fixation point location in the foveal avascular zone. *Invest Ophthalmol Vis Sci.* 1990;31(10):2099–2105.
39. Wilk MA, Dubis AM, Cooper RF, Summerfelt P, Dubra A, Carroll J. Assessing the spatial relationship between fixation and foveal specializations. *Vision Res.* 2017;132:53–61.
40. Bernard JB, Chung STLL. Visual acuity is not the best at the preferred retinal locus in people with macular disease. *Optom Vis Sci.* 2018;95(9):829–836.
41. Pritchard RM. Stabilized images on the retina. *Sci Am.* 1961;204:72–78.
42. Harmening WM, Tuten WS, Roorda A, Sincich LC. Mapping the perceptual grain of the human retina. *J Neurosci.* 2014;34(16):5667–5677.
43. Poonja S, Patel S, Henry L, Roorda A. Dynamic visual stimulus presentation in an adaptive optics scanning laser ophthalmoscope. *J Refract Surg.* 2005;21(5):S575–S580.
44. Grieve K, Tiruveedhula P, Zhang Y, Roorda A. Multi-wavelength imaging with the adaptive optics scanning laser ophthalmoscope. *Opt Express.* 2006;14(25):12230–12242.
45. Domdei N, Domdei L, Reiniger JL, et al. Ultra-high contrast retinal display system for single photoreceptor psychophysics. *Biomed Opt Express.* 2018;9(1):157–172.
46. Domdei N, Linden M, Reiniger JL, Holz FG, Harmening WM. Eye tracking-based estimation and compensation of chromatic offsets for multi-wavelength retinal microstimulation with foveal cone precision. *Biomed Opt Express.* 2019;10(8):4126–4141.
47. Dartnall HJ, Bowmaker JK, Mollon JD. Human visual pigments: microspectrophotometric results from the eyes of seven persons. *Proc R Soc London Ser B Biol Sci.* 1983;220(1218):115–130.
48. Atchison DA, Smith G. Chromatic dispersions of the ocular media of human eyes. *J Opt Soc Am A Opt Image Sci Vis.* 2005;22(1):29–37.
49. Harmening WM, Tiruveedhula P, Roorda A, Sincich LC. Measurement and correction of transverse chromatic offsets for multi-wavelength retinal microscopy in the living eye. *Biomed Opt Express.* 2012;3(9):2066–2077.
50. Arathorn DW, Yang Q, Vogel CR, Zhang Y, Tiruveedhula P, Roorda A. Retinally stabilized cone-targeted stimulus delivery. *Opt Express.* 2007;15(21):13731–13744.
51. Cunefare D, Fang L, Cooper RF, Dubra A, Carroll J. Open source software for automatic detection of cone photoreceptors in adaptive optics ophthalmoscopy using convolutional neural networks. *Sci Rep.* 2017;7(1):6620.
52. Reiniger JL, Lobecke AC, Sabesan R, et al. Habitual higher order aberrations affect Landolt but not Vernier acuity. *J Vis.* 2019;19(5):11.
53. Spaide RF, Curcio CA. Anatomical correlates to the bands seen in the outer retina by optical coherence tomography: literature review and model. *Retina.* 2011;31(8):1609–1619.
54. Watson AB, Pelli DG. QUEST: a Bayesian adaptive psychometric method. *Percept Psychophys.* 1983;33(2):113–120.
55. Tuten WS, Harmening WM, Sabesan R, Roorda A, Sincich LC. Spatiochromatic interactions between individual cone photoreceptors in the human retina. *J Neurosci.* 2017;37(39):9498–9509.
56. Meadow A, Sincich LC. Light propagation and capture in cone photoreceptors. *Biomed Opt Express.* 2018;9(11):5543–5565.
57. Guizar-Sicairos M, Thurman ST, Fienup JR. Efficient subpixel image registration algorithms. *Opt Lett.* 2008;33(2):156–158.
58. MacLeod DI, Williams DR, Makous W. A visual nonlinearity fed by single cones. *Vision Res.* 1992;32(2):347–363.
59. Cottaris NP, Jiang H, Ding X, Wandell BA, Brainard DH. A computational-observer model of spatial contrast sensitivity: effects of wave-front-based optics, cone-mosaic structure, and inference engine. *J Vis.* 2019;19(4):8.
60. Cottaris NP, Wandell BA, Rieke F, Brainard DH. A computational observer model of spatial contrast sensitivity: effects of photocurrent encoding, fixational eye movements, and inference engine. *J Vis.* 2020;20(7):17.
61. Bowmaker JK, Dartnall HJ, Lythgoe JN, Mollon JD. The visual pigments of rods and cones in the rhesus monkey, *Macaca mulatta*. *J Physiol.* 1978;274(1):329–348.
62. Agarwal A, Soliman MK, Hanout M, et al. Adaptive optics imaging of retinal photoreceptors overlying lesions in white dot syndrome and its functional correlation. *Am J Ophthalmol.* 2015;160(4):806–816.e2.
63. Supriya D, Shwetha M, Kiran Anupama K, et al. Structural and function correlation of cone packing utilizing adaptive optics and microperimetry. *Biomed Res Int.* 2015;2015:968672.
64. Johnson CA, Keltner JL, Balestry FG. Static and acuity profile perimetry at various adaptation levels. *Doc Ophthalmol.* 1981;50(2):371–388.
65. Khuu SK, Kalloniatis M. Standard automated perimetry: determining spatial summation and its effect on contrast sensitivity across the visual field. *Invest Ophthalmol Vis Sci.* 2015;56(6):3565–3576.
66. Boettner EA, Wolter JR. Transmission of the ocular media. *Invest Ophthalmol Vis Sci.* 1962;1(6):776–783.
67. Bowmaker JK, Dartnall HJ. Visual pigments of rods and cones in a human retina. *J Physiol.* 1980;298(2):501–511.
68. Koenig D, Hofer H. The absolute threshold of cone vision. *J Vis.* 2011;11(1):1–24.
69. Sperling HG, Jolliffe CL. Intensity-time relationship at threshold for spectral stimuli in human vision. *J Opt Soc Am.* 1965;55(2):191–199.
70. Krauskopf J, Mollon JD. The independence of the temporal integration properties of individual chromatic mechanisms in the human eye. *J Physiol.* 1971;219(3):611–623.
71. Reeves A, Wu S, Schirillo J. The effect of photon noise on the detection of white flashes. *Vision Res.* 1998;38(5):691–703.
72. Dacey DM, Petersen MR. Dendritic field size and morphology of midget and parasol ganglion cells of the human retina. *Proc Natl Acad Sci USA.* 1992;89(20):9666–9670.
73. Scoles D, Sulai YN, Langlo CS, et al. In vivo imaging of human cone photoreceptor inner segments. *Invest Ophthalmol Vis Sci.* 2014;55(7):4244–4251.
74. Tuten WS, Tiruveedhula P, Roorda A. Adaptive optics scanning laser ophthalmoscope-based microperimetry. *Optom Vis Sci.* 2012;89(5):563–574.
75. Srinivasan VJ, Monson BK, Wojtkowski M, et al. Characterization of outer retinal morphology with high-speed, ultrahigh-resolution optical coherence tomography. *Invest Ophthalmol Vis Sci.* 2008;49(4):1571–1579.
76. Wilk MA, Wilk BM, Langlo CS, Cooper RF, Carroll J. Evaluating outer segment length as a surrogate measure of peak foveal cone density. *Vision Res.* 2017;130:57–66.
77. Maden G, Cakir A, Icar D, Erden B, Bolukbasi S, Elcioglu M. The distribution of the photoreceptor outer segment length in a healthy population. *J Ophthalmol.* 2017;2017:4641902.
78. Polyak SL. *The Retina*. Chicago, IL: University of Chicago Press; 1941.
79. Yamada E. Some structural features of the fovea centralis in the human retina. *Arch Ophthalmol.* 1969;82(2):151–159.
80. Hoang QV, Linsenmeier RA, Chung CK, Curcio CA. Photoreceptor inner segments in monkey and human retina: mitochondrial density, optics, and regional variation. *Vis Neurosci.* 2002;19(4):395–407.

81. Wu Z, Ayton LN, Luu CD, Guymer RH. Relationship between retinal microstructures on optical coherence tomography and microperimetry in age-related macular degeneration. *Ophthalmology*. 2014;121(7):1445–1452.
82. Asaoka R, Murata H, Yanagisawa M, et al. The association between photoreceptor layer thickness measured by optical coherence tomography and visual sensitivity in glaucomatous eyes. *PLoS One*. 2017;12(10):1–12.
83. Baylor DA, Lamb TD, Yau KW. The membrane current of single rod outer segments. *J Physiol*. 1979;288(1):589–611.
84. Allphin M, Cava J, Cooper RF, Carroll J. Reevaluating outer segment length as a surrogate for peak cone density. *Invest Ophthalmol Vis Sci*. 2020;61(7):204.
85. Bedggood P, Metha A. Variability in bleach kinetics and amount of photopigment between individual foveal cones. *Invest Ophthalmol Vis Sci*. 2012;53(7):3673–3681.
86. Sincich LC, Sabesan R, Tuten WS, Roorda A, Harmening WM. Functional imaging of cone photoreceptors. In: Kremers J, Baraas RC, Marshall NJ, eds. *Human Color Vision*. Cham, Switzerland: Springer International Publishing; 2016:71–104.
87. Schnapf JL, Kraft TW, Baylor DA. Spectral sensitivity of human cone photoreceptors. *Nature*. 1987;325(6103):439–441.
88. Schnapf JL, Nunn BJ, Meister M, Baylor DA. Visual transduction in cones of the monkey *Macaca fascicularis*. *J Physiol*. 1990;427:681–713.
89. Deeb SS. The molecular basis of variation in human color vision. *Clin Genet*. 2005;67(5):369–377.
90. Chichilnisky EJ, Baylor DA. Receptive-field microstructure of blue-yellow ganglion cells in primate retina. *Nat Neurosci*. 1999;2(10):889–893.
91. Field GD, Gauthier JL, Sher A, et al. Functional connectivity in the retina at the resolution of photoreceptors. *Nature*. 2010;467(7316):673–677.
92. Li PH, Field GD, Greschner M, et al. Retinal representation of the elementary visual signal. *Neuron*. 2014;81(1):130–139.
93. Freeman J, Field GD, Li PH, et al. Mapping nonlinear receptive field structure in primate retina at single cone resolution. *Elife*. 2015;4:1–21.
94. Liu JK, Schreyer HM, Onken A, et al. Inference of neuronal functional circuitry with spike-triggered non-negative matrix factorization. *Nat Commun*. 2017;8(1):149.
95. Thoreson WB, Mangel SC. Lateral interactions in the outer retina. *Prog Retin Eye Res*. 2012;31(5):407–441.
96. Curcio CA, Allen KA, Sloan KR, et al. Distribution and morphology of human cone photoreceptors stained with anti-blue opsin. *J Comp Neurol*. 1991;312(4):610–624.
97. Bumsted K, Hendrickson A. Distribution and development of short-wavelength cones differ between *Macaca* monkey and human fovea. *J Comp Neurol*. 1999;403(4):502–516.
98. Ahnelt PK. The photoreceptor mosaic. *Eye (Lond)*. 1998;12(3):531–540.
99. Palczewska G, Vinberg F, Stremplewski P, et al. Human infrared vision is triggered by two-photon chromophore isomerization. *Proc Natl Acad Sci USA*. 2014;111(50):E5445–E5454.

Amended August 4, 2021: In the first sentence of the Methods, “PRL of fixation were mapped with cellular precision” was changed to “PRL were mapped with cellular precision,” and Reference 9 was changed from Reiniger JL, Domdei N, Holz FG, Harmening WM. Human gaze is precisely aligned with the foveolar cone topography of both eyes [preprint]. *bioRxiv*, <https://doi.org/10.1101/2021.03.19.436115> to Reiniger JL, Domdei N, Holz FG, Harmening WM. Human gaze is systematically offset from the center of cone topography. *Curr Biol*. 2021;31:1–6, <https://doi.org/10.1016/j.cub.2021.07.005>.